Improving the dispersoid distribution and recrystallization resistance of a Zr-containing 6xxx alloy using two-step homogenization

A. Elasheri [a,*], E.M. Elgallad [a], N. Parson [b], X.-G. Chen [a]

[a] Department of Applied Science, University of Quebec at Chicoutimi, Saguenay (QC), Canada G7H 2B1

[b] Arvida Research and Development Centre, Rio Tinto Aluminium, Saguenay (QC), Canada G7S 4K8

(*Corresponding author: ali.elashery1@uqac.ca)

Abstract

Two-step homogenization was applied to a 6xxx alloy containing Zr to enhance the characteristics of Zr-bearing dispersoids and recrystallization resistance. The two-step homogenization treatments were composed of a first step at 400 °C for 48 h and a second step at 500 °C for 2 and 5 h and compared with single-step homogenization conducted at 500 °C for 2 and 5 h. The dispersoid microstructure was characterized using optical microscopy and scanning and transmission electron microscopies. The thermomechanical simulator Gleeble 3800 was used to conduct the hot compression tests at 350°C/1.0s^{-1}. To study the recrystallization resistance, post-deformation annealing at 500 °C for 1 h was performed on the deformed samples. The grain structure after deformation and annealing was characterized based on the EBSD technique. The results showed that compared to single-step homogenization, the dispersoid characteristics were significantly improved using two-step homogenization, where the number density of $L1_2$-Al_3Zr dispersoids increased by 75 to 145% while their size decreased by 9 to 25% and the distribution of the DO_{22}-$(Al, Si)_3(Zr,Ti)$ dispersoids became more uniform. The improved characteristics of Zr-bearing dispersoids and the narrower dispersoid-free zones produced by the two-step homogenization significantly improved the recrystallization resistance with a reduction in the recrystallized area fraction reached 85% when compared with single-step homogenization.

Keywords

Al-Mg-Si 6xxx alloy; homogenization treatment; Zr-bearing dispersoids; flow stress; recrystallization resistance.

1. Introduction

The homogenization treatment is a primary thermal process applied after direct chill (DC) casting of Al-Mg-Si 6xxx aluminium alloys. The purposes of this treatment are the re-distribution of the alloying elements to overcome the microsegregation, dissolution of the low-melting eutectic phases and refinement of the large intermetallic particles. Therefore, a high-temperature homogenization (500 - 550 °C) is commonly used to achieve such purposes. Subsequently, the homogenized material undergoes a thermo-mechanical process (rolling, extrusion, and forging) to achieve the desired shape and mechanical properties. However, recrystallization of the deformed structure may occur, which can negatively affect the mechanical and corrosion resistance properties for some products [1, 2]. Therefore, maintaining a fibrous deformed structure during the thermo-mechanical process and its subsequent heat treatment (solutionizing or annealing) is advantageous [3].

Introducing thermally stable dispersoids during homogenization is an effective way to retard dislocation motion and sub-grain boundary migration and inhibit recrystallization. Zirconium is a common microalloying element among the other transition elements with limited solubility and extremely low diffusivity in the aluminum matrix [4, 5]. During homogenization, Zr can form nano-sized Al_3Zr dispersoids, which are thermally stable and coherent with the aluminum matrix, and therefore effectively retard the recrystallization [6, 7]. However, the homogenization temperature significantly affects the dispersoid characteristics. Higher temperatures lead to

precipitation of large dispersoids with a low number density, while denser dispersoids with smaller sizes could be obtained by low-temperature homogenization. Therefore, adjusting the homogenization parameters is crucial for optimizing the dispersoids characteristics in terms of number density and size to achieve an adequate inhibition of recrystallization.

According to the Zener drag force and its pinning effect [8], a large volume fraction and small dispersoid size lead to a higher retarding effect on the recrystallization. In addition, a uniform distribution is also important to apply an even pinning effect in the aluminum matrix [9]. Due to the segregation of Zr to the dendrite centers during solidification, only a few dispersoids with relatively large sizes are precipitated in the interdendritic regions. Thus, these regions are prone to recrystallize more readily than dendrite centers. Two-step homogenization is a promising approach that effectively improves the precipitation and the distribution of the Al_3Zr dispersoids [6, 10-14]. The first step is commonly conducted at a low temperature for a relatively long holding time to promote the nucleation of dispersoids, while the second step is conducted at a high temperature to complete the homogenization conventionally but for a short holding time to prevent the excessive growth of the dispersoids. It was reported [6] that finer Al_3Zr dispersoids with higher density were observed in AA7150 alloys for two-step homogenization as compared to the single-step homogenization. Consequently, superior recrystallization resistance was achieved in 7xxx alloys after two-step homogenization due to the denser Al_3Zr dispersoids[5, 6, 10, 12, 13]. Improved recrystallization resistance and strength after two-step homogenization were also reported for Al–Cu 2xxx alloys [14] due to the fine and dense Al_3Zr.

Although a number of studies applied multi-step homogenization to improve the characteristics of Zr-bearing dispersoids in specific aluminum alloy systems, such as 2xxx and 7xxx, there is a lack of research work relating to Al-Mg-Si 6xxx series. In addition, static

recrystallization may occur during post-deformation heat treatment by migration of grain boundaries [15]. Therefore, this study examined the effect of two-step homogenization on the precipitation of Zr-bearing dispersoids and recrystallization resistance in an Al-0.3Mg-0.4Si-0.15Zr alloy in comparison with a single-step treatment. The dispersoids were characterized using optical microscopy and scanning and transmission electron microscopies. Hot compression tests were conducted at 350°C/1.0s^{-1} on homogenized samples using a Gleeble 3800 thermomechanical simulator. In order to evaluate the recrystallization resistance, high-temperature annealing (500°C/1h) was carried out on the deformed samples, and the resulting microstructures were investigated using EBSD techniques.

2. Experimental procedures

An Al-Mg-Si alloy containing Zr was prepared using pure Al (99.7 wt.%) and pure Mg (99.8 wt.%) as well as Al-50 wt.% Si, Al-25 wt.% Fe, and Al-15 wt.% Zr master alloys. The actual chemical composition of the alloy analyzed using optical emission spectroscopy is listed in Table 1. The material was melted using an electrical resistance furnace and maintained at ~750°C for 30 min. Then, 0.13 wt.% Ti in the form of Al-5Ti-1B master alloy was added into the melt as a grain refiner. The melt was poured into a rectangular permanent steel mold with dimensions of 30 mm × 40 mm × 80 mm. The cast ingots were then subjected to single-step and two-step homogenization treatments, as shown by the schematic diagrams in Fig. 1. The single-step treatments were performed at 500 °C for 2 h and 5 h. The two-step treatments included a first step at 400 °C for 48 h and a second step at 500 °C for 2 h and 5 h. The samples were subjected to direct water quenching to room temperature after homogenization. In addition, a few samples were water quenched after the first step (400°C/48h).

Uniaxial hot compression tests were performed on a Gleeble 3800 thermomechanical simulator using cylindrical samples with a diameter of 10 mm and a length of 15 mm. The compression tests involved heating the samples to the deformation temperature of 350 °C at a heating rate of 2 °C/s and then holding for 3 minutes to ensure a uniform temperature distribution. The samples were deformed with a constant strain rate of 1.0 s^{-1} to a true strain of 0.7, followed by water quenching to room temperature to retain the deformed microstructure. To study the recrystallization process after the post-deformation heat treatment, the deformed samples were annealed at 500 ºC for 1 h, followed by water quenching to room temperature.

To study the microstructure, the homogenized samples were polished using standard metallographic methods. The intermetallic phases and dispersoids were observed using an optical microscope (Nikon, Eclipse ME600) and a scanning electron microscope (SEM, JEOL-6480LV) after etching by 0.5% HF for 30 seconds. In addition, a transmission electron microscope (TEM, JEM−2100) operated at 200 kV was used to observe the fine Zr-bearing dispersoids in detail. The TEM samples were mechanically ground and then electropolished using a twin-jet electropolisher operated at 20 V and -20°C in a 30 vol.% nitric acid and 70 vol.% methanol solution. The samples were observed in the dark and bright field modes along the <001> zone axis of the Al matrix to reveal the dispersoids. The average dispersoid size and number density were measured based on image analysis of TEM images and foil thickness.

The microstructures after deformation and after post-deformation annealing were characterized using EBSD analysis. The EBSD samples were sectioned parallel to the deformation axis along the centerline and then carefully polished to obtain high indexing quality. For an accurate comparison, the central region of the samples was examined for all conditions. Orientation maps were produced with a step size of 3 μm for grain structure and a fine step size of 0.5 μm to reveal

more details on the grain and subgrain structures and to measure the misorientation distribution. The low angle (2-5), medium angle (5-15º), high angle (>15º), and original grain boundaries (>30º) were presented by white, green, thin black, and solid black lines, respectively. Misorientation angles below 2º were not considered to avoid the microstructure noise caused by sample preparation. In addition, grain orientation spread (GOS) maps were plotted to reveal any recrystallized grains using MTEX, a comprehensive open-source freely available MATLAB toolbox. A threshold value of 2º was used to distinguish between recrystallized and deformed grains. The EBSD analysis and GOS maps are adopted here as common characterization techniques being used to reveal directly and independently the changes in the grain structure. These techniques are preferred over mechanical testing methods, such as microhardness and tensile tests, because the results of these methods could be affected by other factors besides the grain structure and would therefore be misleading in revealing the sole effect of the latter.

3. Results and discussion

3.1. Dispersoid Microstructure

3.1.1. Precipitation of $L1_2$-Al_3Zr dispersoids

The dark field TEM images presented in Fig. 2 show the dispersoid microstructure within the dispersoid zones in different homogenization conditions. The dispersoids appeared in these images were identified to be $L1_2$-Al_3Zr dispersoids based on their morphology and the crystal structure, as was confirmed by corresponding selected area electron diffraction patterns (SAEDPs) [16]. As an example, the SAEDP corresponding to the image shown in Fig. 2a is given in its inset. The characteristics of the Al_3Zr dispersoids in terms of the number density and size varied from one homogenization condition to another. As can be seen in Fig. 2a, the first step at 400 ºC for 48

h resulted in a dense distribution of dispersoids with a very fine size. On the other hand, the single-step homogenization at 500 ºC, whether after holding for 2 or 5 h (Fig. 1b and c), resulted in a lower density of coarser dispersoids. The two-step homogenization treatments, however, improved the dispersoid characteristics as compared with the single-step homogenization at 500 ºC (Fig. 2d and e *vs*. Fig. 2b and c).

The number density and the size of Al_3Zr dispersoids were measured for all homogenization conditions and are listed in Table 2 for comparison. A high number density of 2841 μm^{-3} with a size of 9 nm was obtained by the first step of 400ºC/48h. The number density decreased significantly to ~950 μm^{-3} while the size increased to 14 nm for both single-step 500 ºC treatments. On the other hand, the two-step homogenization of 400°C/48h + 500°C/2h resulted in much better dispersoid characteristics compared to the single-step homogenization of 500°C/2h by increasing the number density to 2315 μm^{-3} and decreasing the size to 9.2 nm. In comparison, increasing the holding time to 5 h in the second step coarsened the dispersoids and decreased their number density. However, the dispersoid characteristics in this condition were still remarkably better relative to the single-step homogenization of 500°C/5h (Table 2).

In general, during homogenization, the Al_3Zr dispersoids precipitate out of the α-Al solid solution enriched with Zr solutes during solidification [17]. The variation of the Al_3Zr characteristics is mainly controlled by the homogenization temperature and time. The relatively low homogenization temperature of 400 °C promoted the formation of abundant dispersoid nuclei. Prolonging the holding time at this temperature up to 48 h allowed the growth of these nuclei progressively to dense and fine Al_3Zr dispersoids. The growth of these dispersoids was, however, restricted owing to the low diffusion rate of Zr at 400 ºC. On the other hand, the higher

homogenization temperature of 500 ºC diminished the dispersoid nucleation rate but increased the Zr diffusion rate and consequently the growth rate, leading to a sparse dispersion of coarse Al_3Zr dispersoids. Thus, by conducting the first step of the two-step homogenization at 400 ºC for 48 h, the nucleation of fine Al_3Zr dispersoids was enhanced compared to the single-step homogenization at 500 ºC, resulting in a higher number density of Al_3Zr dispersoids with a smaller size for both two-step homogenization conditions. Conducting the second step at 500 ºC, whether for 2 or 5 h, coarsened the fine dispersoids formed during the first step. However, it could, on the other hand, satisfy the industrial requirements of 6xxx alloys prior to hot deformation processes by dissolving the eutectic phases and decreasing the microsegregation.

The equilibrium partition coefficient of Zr during solidification in Al is greater than unity (k_0 ~2.5) [18]. Therefore, Zr segregates towards the dendrite centers during solidification, resulting in an enrichment of Zr in these regions. On the other hand, the supersaturation level of Zr is much lower at the dendrite/grain boundaries, which limits the precipitation of Al_3Zr dispersoids, resulting in the appearance of dispersoid free zones (DFZs). Fig. 3a and b show the DFZs for the single-step (500°C/2h) and two-step (400°C/48h + 500°C/2h) homogenization conditions, respectively. As can be seen, generally wide DFZs (> 2 µm) were observed in the case of the single-step homogenization (Fig. 3a), while the two-step homogenization resulted in much narrower DFZs (< 1 µm, Fig. 3b). This observation was further confirmed using other TEM images (see Supplementary Material, Fig. S3). The first step at 400 °C provides a high driving force for the nucleation of dispersoids [19, 20], especially for the regions adjacent to grain boundaries with a low Zr concentration. Therefore, a higher number density of dispersoids was found close to grain boundaries after the two-step homogenization, resulting in narrower DFZs and an overall improvement in the dispersoid distribution.

3.1.2. Precipitation of DO_{22}-$(Al,Si)_3(Zr,Ti)$ dispersoids

In addition to the fine spherical $L1_2$-Al_3Zr dispersoids, much larger elongated dispersoids (~ 100 nm) were also detected in the single-step and two-step homogenization conditions (Fig. 4a), containing Al, Zr and Si as well as a trace of Ti (Fig. 4b). Based on the TEM-EDS analysis, these dispersoids were identified as DO_{22}-$(Al,Si)_3(Zr,Ti)$ dispersoids [21], which have been reported to form in the presence of Si and Ti [22, 23].

The distribution of the DO_{22}-$(Al,Si)_3(Zr,Ti)$ dispersoids could not be properly observed by TEM due to their relatively large size and interspaces. The quantitative analysis of these dispersoids based on TEM images could not also be made due to their non-homogeneous distribution and very low number density in the alloy studied. However, contrary to the nanoscale $L1_2$-Al_3Zr dispersoids, the distribution of DO_{22} dispersoids could be revealed after etching by optical microscopy in the dark-field mode and SEM (Fig. 5). As can be seen, the precipitation of DO_{22} dispersoids occurred near grain boundaries with the single-step 500°C/5h homogenization (Fig. 5a-c), but occurred in the grain cores with a more uniform distribution with the two-step 400ºC/48h + 500ºC/5h homogenization (Fig. 5d-f). This can be attributed to the initial distribution of Si, which promotes the DO_{22} dispersoids [21]. For the single-step 500 ºC homogenization, a large amount of Si was initially segregated at grain boundaries after casting [24], thereby promoting the precipitation of DO_{22} dispersoids in the grain boundary areas. On the other hand, the first step of 400°C/48h as part of the two-step treatment enhanced the diffusion of Si inside the grains, resulting in a more uniform distribution of DO_{22} dispersoids in the grain cores. The EDS analysis was used to evaluate the Si concentration in the α-Al matrix near grain boundaries and inside the grains in the single- and two-step homogenization conditions. However, due to the

limitation of the EDS to detect slight differences of Si concentration, no appreciable differences were revealed between these conditions.

3.2. Flow stress

Fig. 6 shows the compression flow curves at 350 °C and a strain rate of 1.0 s^{-1} for different homogenization treatments. For all conditions, the flow stress increased sharply by the intense work hardening at the beginning of compression, and then continued to rise at a lower rate with increasing strain, indicating the domination of the work hardening over the effect of softening mechanisms.

Generally, the flow stress was controlled by both dispersoid and solid solution strengthening effects and the latter was more dominant. The first step of 400ºC/48h produced fine, dense $L1_2$-Al_3Zr dispersoids. However, the relatively low temperature did not allow the dissolution of the equilibrium β-Mg_2Si precipitates, which decreased the supersaturation levels of Mg and Si in the α-Al and consequently the solid solution strengthening, leading to the lowest flow stress in this condition. In comparison, the single-step homogenization at 500 ºC for 2 or 5 h moderately increased the flow stress, where the solid solution strengthening was increased by the enhanced dissolution of β-Mg_2Si precipitates at the higher temperature, while a reduced amount of fine $L1_2$ dispersoids was precipitated in combination with large DO_{22} dispersoids. Both two-step homogenization treatments, which combined between enhanced dispersoid characteristics and high solid solution strengthening, exhibited the highest flow stresses. The dissolution of β-Mg_2Si precipitates and the resulting increase in the degree of the supersaturation of the α-Al solid solution in all 500 ºC homogenization conditions were both confirmed using microstructure observations and electrical conductivity measurements (see Supplementary Material, Figs. S1 and S2).

3.3. Recrystallization resistance

After the hot compression tests, the deformed samples were annealed at 500 ºC for 1 h to evaluate the recrystallization resistance. Fig. 7 shows the grain spread orientation maps (GOS) for the single-step and two-step homogenization conditions as well as the as-cast condition (no prior homogenization before deformation). In addition, the recrystallized area fractions were measured and plotted in Fig. 8. The determination of recrystallized grains was based on the GOS parameter, which can be considered as an indication of the dislocation densities and strain level in the individual grain [25]. The grain structures with a GOS value less than 2° have a lower strain level and are considered recrystallized structures [26, 27]. On the other hand, the deformed structure usually possesses higher GOS values (> 5°). After annealing, the samples exhibited different degrees of recrystallization depending on the material condition before deformation. For the as-cast material, the microstructure was highly recrystallized (Fig. 7a) with an area percentage of 70.4% due to the absence of dispersoids. Moreover, the majority of the remaining deformed structure showed low GOS values (less than 4°). In contrast, much lower degrees of recrystallization were observed in the homogenized samples, depending on the homogenization condition, due to the precipitation of thermally stable dispersoids that could hinder the dislocation motion. The lowest degree of recrystallization was exhibited by the 400°C/48h first step treatment (Fig. 7b) with a recrystallized area fraction of only 14%. In contrast, single-step homogenization at 500 °C resulted in higher degrees of recrystallization (Fig. 7c and d) with recrystallized area fractions of 29 and 27% after holding for 2 and 5 h, respectively. On the other hand, the recrystallization process was almost completely inhibited by the two-step homogenization of 400°C /48h + 500°C /2h (Fig.7e) with only 4% recrystallized area fraction. In addition, most of the deformed regions showed high GOS values (> 8°), indicating a less recovered structure. However,

increasing the holding time of the second step to 5 h negatively affected the recrystallization resistance, increasing the recrystallized area fraction to 20% but with high GOS values (>10, Fig. 7f). The recrystallization resistance in this case was still, however, better than that obtained after single-step homogenization at 500 °C whether for 2 or 5 h (20% *vs*. 29% and 27% recrystallized area fraction).

The samples homogenized by the single-step 500°C/2h and two-step 400°C/48h + 500°C/2h treatments were selected for further microstructural analysis. All-Euler maps shown in Fig. 9 reveal the evolution of different grains and their boundaries for both samples before and after annealing. In addition, the distribution and the quantitative analysis of the misorientation angles are presented in Fig. 10. The as-deformed structure in both homogenization cases (Fig. 9a and b) showed typically elongated fibrous grains with high densities of low and medium angle boundaries, indicating a dynamically recovered structure. However, as shown in Fig. 10a and b, a much higher fraction of low-angle boundaries (LAB) with a lower mean misorientation angle was associated with the two-step homogenization compared with the single-step homogenization (84.6 % *vs*. 65.8 % and 9.6° *vs*. 15.4°, respectively). Such results indicate that dynamic recovery during hot deformation was slower after two-step homogenization. Moreover, some small equiaxed grains were observed along grain boundaries in the case of the single-step homogenization (arrowed in Fig. 9a).

After annealing, a significant difference in the microstructure was observed between the single-step and two-step treatments. Single-step homogenization (Fig. 9c) resulted in some large recrystallized grains along grain boundaries, indicating severe growth of the pre-existing grains observed after deformation. In contrast, the two-step homogenization only exhibited a dynamically recovered structure with some development of low angle boundaries (white lines) into medium-

angle boundaries (green lines). The high annealing temperature (500 °C) facilitates dislocation motion and annihilation and, subsequently, dynamic recovery. These results are confirmed by the distribution of the misorientation angles (Fig. 10c and d), showing a higher fraction of LAB after two-step homogenization compared with the single-step homogenization (74.6 % *vs*. 60.1 %).

It has been demonstrated that the coherent Al_3Zr dispersoids can substantially retard dislocation movement and subgrain boundary migration during thermal treatment [28]. The volume fraction and size of dispersoids determine the amount of the Zener pinning pressure on the grain boundaries [8]. The pinning pressure can be increased by maximizing the volume fraction of dispersoids and minimizing their size. The two-step homogenization could achieve such a combination due to the higher number density of fine Al_3Zr dispersoids. Consequently, a less recovered structure, which was represented by a higher fraction of low angle boundaries, was obtained after deformation with the two-step homogenization compared with the single-step homogenization. Moreover, static recovery was also limited during annealing, in the case of the two-step homogenization.

The distribution of dispersoids also plays a crucial role in recrystallization resistance. The nonuniform distribution of dispersoids leads to the formation of dispersoid-free zones adjacent to grain boundaries (Fig. 3). In addition, the large intermetallic particles formed along the grain boundaries after solidification could promote the recrystallization via particle stimulated nucleation mechanism [29]. Such microstructural features lead to more rapid recrystallization in these regions compared to the grain interiors. The single-step homogenization exhibited wide DFZs depleted of $L1_2$-Al_3Zr dispersoids, as shown in Fig. 3a. In addition, a nonuniform distribution of DO_{22}-$(Al,Si)_3(Zr,Ti)$ dispersoids was observed (Fig. 5a to c), though this dispersoid-type was reported to have less effect on recrystallization compared to the $L1_2$ type [30, 31]. As a

result, some small recrystallized grains were observed after deformation along the grain boundaries (Fig. 9a). Later, these small grains were able to grow and coarsen during annealing due to the insufficient pinning force in the DFZs. In contrast, the two-step homogenization provided a more uniform distribution of both $L1_2$-Al_3Zr and DO_{22}-$(Al,Si)_3(Zr,Ti)$ dispersoids, resulting in narrower DFZs. As a result, a significant improvement in the recrystallization resistance was observed after hot deformation or after annealing.

4. Conclusions

A two-step homogenization practice was applied to improve the dispersoid distribution and recrystallization resistance of a Zr-containing 6xxx alloy. From the results obtained, the following conclusions could be drawn:

1. The characteristics of Zr-bearing dispersoids were significantly improved by the two-step homogenization. The number density of $L1_2$-Al_3Zr dispersoids increased by 75 to 145%, while their size decreased by 9 to 25% compared with the single-step homogenization.
2. Large DO_{22}-$(Al,Si)_3(Zr,Ti)$ dispersoids were precipitated near the grain boundaries after the single-step homogenization. However, the distribution of such dispersoids was more uniform in the aluminum matrix after the two-step homogenization.
3. The two-step homogenization and the single-step 500 °C homogenization dissolved β-Mg_2Si particles almost completely, resulting in nearly similar supersaturation levels of α-Al solid solution, and would consequently have similar solid solution strengthening effects on the flow stress. Thus, the higher flow stress obtained in the two-step homogenization condition could be attributed to the enhanced characteristics of Al_3Zr dispersoids and the more uniform distribution of $(Al,Si)_3(Zr,Ti)$ dispersoids in this condition.

4. The improved distribution of Zr-bearing dispersoids and the narrower dispersoid-free zones produced by two-step homogenization significantly improved the recrystallization resistance during post-deformation annealing, resulting in a reduction in the recrystallized area fraction reached 85% when compared with the single-step homogenization.

Acknowledgments

The authors would like to acknowledge the financial support of the Natural Sciences and Engineering Research Council of Canada (NSERC) under the Grant No. CRDPJ 514651-17 and Rio Tinto Aluminum through the Research Chair in the Metallurgy of Aluminum Transformation at University of Quebec at Chicoutimi.

References

[1] G.S. Peng, K.H. Chen, H.C. Fang, S.Y. Chen, and H. Chao, *The effect of recrystallization on corrosion and electrochemical behavior of 7150 Al alloy*, Mater. Corros. 62 (2011), pp. 35-40.

[2] Y. Birol, *Effect of Cr and Zr on the grain structure of extruded EN AW 6082 alloy*, Met. Mater. Int. 20 (2016), pp. 727-732.

[3] C. Poletti, T. Wójcik, and C. Sommitsch, *Hot Deformation of AA6082 Containing Fine Intermetallic Particles*, Metall. Mater. Trans. A 44 (2012), pp. 1577-1586.

[4] K.E. Knipling, D.C. Dunand, and D.N. Seidman, *Precipitation evolution in Al–Zr and Al–Zr–Ti alloys during aging at 450–600°C,* Acta Mater. 56 (2008), pp. 1182-1195.

[5] Z. Jia, G. Hu, B. Forbord, and J.K. Solberg, *Enhancement of recrystallization resistance of Al–Zr–Mn by two-step precipitation annealing*, Mater. Sci. Eng., A 483-484 (2008), pp. 195-198.

[6] Z. Guo, G. Zhao, and X.G. Chen, *Effects of two-step homogenization on precipitation behavior of Al3Zr dispersoids and recrystallization resistance in 7150 aluminum alloy*, Mater. Charact. 102 (2015), pp. 122-130.

[7] H. Li, Z. Gao, H. Yin, H. Jiang, X. Su, and J. Bin, *Effects of Er and Zr additions on precipitation and recrystallization of pure aluminum*, Scripta Mater. 68 (2013), pp. 59-62.

[8] E. Nes, N. Ryum, and O. Hunderi, *On the Zener drag*, Acta Metall. 33 (1985), pp. 11-22.

[9] Z. Xie, Z. Jia, K. Xiang, Y. Kong, Z. Li, X. Fan, W. Ma, H. Zhang, L. Lin, K. Marthinsen, and Q. Liu, *Microstructure Evolution and Recrystallization Resistance of a 7055 Alloy Fabricated by Spray Forming Technology and by Conventional Ingot Metallurgy*, Metall. Mater. Trans. A 51 (2020), pp. 5378-5388.

[10] Z. Guo, G. Zhao, and X.G. Chen, *Effects of homogenization treatment on recrystallization behavior of 7150 aluminum sheet during post-rolling annealing*, Mater. Charact. 114 (2016), pp. 79-87.

[11] Y. Deng, J. Xu, J. Chen, and X. Guo, *Effect of double-step homogenization treatments on the microstructure and mechanical properties of Al–Cu–Li–Zr alloy*, Mater. Sci. Eng., A 795 (2020).

[12] X.-y. LÜ, E.-j. Guo, P. Rometsch, and L.-j. Wang, *Effect of one-step and two-step homogenization treatments on distribution of Al3Zr dispersoids in commercial AA7150 aluminium alloy*, Trans. Nonferrous Met. Soc. China 22 (2012), pp. 2645-2651.

[13] J.D. Robson, *Optimizing the homogenization of zirconium containing commercial aluminium alloys using a novel process model*, Mater. Sci. Eng., A 338 (2002), pp. 219-229.

[14] Q. Liu, G. Fan, Z. Tan, Z. Li, D. Zhang, J. Wang, and H. Zhang, *Precipitation of Al3Zr by two-step homogenization and its effect on the recrystallization and mechanical property in 2195 Al–Cu–Li alloys*, Mater. Sci. Eng., A 821 (2021).

[15] H.J. McQueen, S. Spigarelli, M.E. Kassner, and E. Evangelista, *Hot Deformation and Processing of Aluminum Alloys*, CRC Press, 2016.

[16] Y. Li, B. Lu, W. Yu, J. Fu, G. Xu, and Z. Wang, *Two-stage homogenization of Al-Zn-Mg-Cu-Zr alloy processed by twin-roll casting to improve L12 Al3Zr precipitation, recrystallization resistance, and performance*, J. Alloys Compd. 882 (2021).

[17] K.E. Knipling, D.C. Dunand, and D.N. Seidman, *Precipitation evolution in Al–Zr and Al–Zr–Ti alloys during isothermal aging at 375–425 C*, Acta Mater. 56 (2008), pp. 114-127.

[18] R. Nadella, D. Eskin, Q. Du, and L. Katgerman, *Macrosegregation in direct-chill casting of aluminium alloys*, Prog. Mater Sci. 53 (2008), pp. 421-480.

[19] A.G. Mochugovskiy, A.V. Mikhaylovskaya, N.Y. Tabachkova, and V.K. Portnoy, *The mechanism of L12 phase precipitation, microstructure and tensile properties of Al-Mg-Er-Zr alloy*, Mater. Sci. Eng., A 744 (2019), pp. 195-205.

[20] P.H.L. Souza, C.A.S.d. Oliveira, and J.M.d.V. Quaresma, *Precipitation hardening in dilute Al–Zr alloys*, J. Mater. Res. Technol. 7 (2018), pp. 66-72.

[21] L. Litynska, D. Abou-Ras, G. Kostorz, and J. Dutkiewicz, *TEM and HREM study of Al3Zr precipitates in an Al-Mg-Si-Zr alloy*, J Microsc 223 (2006), pp. 182-4.

[22] S. Tsunekawa, and M.E. Fine, *Lattice parameters of Al3 (ZrxTi1-x) vs. x in Al-2 at.% (Ti + Zr) alloys*, Scr. metall. mater 16 (1982), pp. 391-392.

[23] Z.-H. Jia, J.-P. Couzinié, N. Cherdoudi, I. Guillot, L. Arnberg, P. Åsholt, S. Brusethaug, B. Barlas, and D. Massinon, *Precipitation behaviour of Al3Zr precipitate in Al–Cu–Zr and Al–Cu–Zr–Ti–V alloys*, Trans. Nonferrous Met. Soc. China 22 (2012), pp. 1860-1865.

[24] H. Seo, J. Gu, K. Park, Y. Jung, J. Lee, and W. Chung, *Solidification and segregation behaviors in 6061 aluminum alloy*, Met. Mater. Int. 19 (2013), pp. 433-438.

[25] W. Wang, and A. Alfantazi, *Correlation between grain orientation and surface dissolution of niobium*, Appl. Surf. Sci. 335 (2015), pp. 223-226.

[26] J. Li, X. Wu, L. Cao, B. Liao, Y. Wang, and Q. Liu, *Hot deformation and dynamic recrystallization in Al-Mg-Si alloy*, Mater. Charact. 173 (2021), p. 110976.

[27] R. Luo, Y. Cao, H. Bian, L. Chen, C.-T. Peng, F. Cao, L. Ouyang, Y. Qiu, Y. Xu, A. Chiba, and X. Cheng, *Hot workability and dynamic recrystallization behavior of a spray formed 7055 aluminum alloy*, Mater. Charact. 178 (2021), p. 111203.

[28] C. Shi, and X.-G. Chen, *Effect of Zr addition on hot deformation behavior and microstructural evolution of AA7150 aluminum alloy*, in *Mater. Sci. Eng., A*, 2014, pp. 183-193.

[29] Q. Zang, H. Yu, Y.-S. Lee, M.-S. Kim, and H.-W. Kim, *Effects of initial microstructure on hot deformation behavior of Al-7.9Zn-2.7Mg-2.0Cu (wt%) alloy*, Mater. Charact. 151 (2019), pp. 404-413.

[30] A. Elasheri, E.M. Elgallad, N. Parson, and X.G. Chen, *Evolution of Zr-Bearing Dispersoids during Homogenization and Their Effects on Hot Deformation and Recrystallization Resistance in Al-0.8%Mg-1.0%Si Alloy*, J. Mater. Eng. Perform. 30 (2021), pp. 7851-7862.

[31] A. Elasheri, E.M. Elgallad, N. Parson, and X.-G. Chen, *Effect of Si Level on the Evolution of Zr-bearing Dispersoids and the Related Hot Deformation and Recrystallization Behaviors in Al-Si-Mg 6xxx Alloys*, Adv. Eng. Mater. (2022).

Figure Captions

Fig. 1. Schematic diagrams of the homogenization treatments, (a) single-step and (b) two-step treatments.

Fig. 2. TEM dark-field images of Al_3Zr dispersoids formed in the dispersoid zones after different homogenization treatments: (a) 400°C/48h (first step), (b) 500°C/2h, (c) 500°C/5h, (d) 400°C/48h + 500°C/2h and (e) 400°C/48h + 500°C/5h.

Fig. 3. Bright field TEM images near grain boundaries showing the width of DFZs in, (a) single-step 500°C/2h, and (b) two-step 400°C/48 h + 500°C/2h homogenization conditions. The Fe-intermetallic in (a) was identified as the plate-like β-AlFeSi intermetallic phase (see Fig. S4 in Supplementary Material).

Fig. 4. (a) Bright field TEM image showing the elongated DO_{22}-$(Al,Si)_3(Zr,Ti)$ dispersoids and (b) the corresponding TEM-EDS spectrum.

Fig. 5. Optical dark field and SEM images showing the distribution of the DO_{22}-$(Al,Si)_3(Zr,Ti)$ dispersoids for single-step 500ºC/5h (a-c) and two-step 400ºC/48h + 500ºC/5h (d-f) treatments.

Fig. 6. Typical flow stress curves after deformation at 350 °C and 1.0 s^{-1} in different homogenization conditions.

Fig. 7. Grain spread orientation maps for different alloy conditions after deformation at 350 °C and 1.0 s^{-1} and annealing at 500 °C for 1 h.

Fig. 8. Recrystallization area fraction for different alloy conditions after deformation at 350 °C

and 1.0 s^{-1} and annealing at 500 °C for 1 h.

Fig. 9. All-Euler orientation maps of as-deformed (a, b) and annealed (c, d) grain structures for the single-step homogenization of 500°C/2h (a, c) and the two-step homogenization of 400°C/48h + 500°C/2h (b, d). Low angle (2°-5°), medium angle (6°-15°), and high angle boundaries (>15°) are represented by white, green, and black lines, respectively.

Fig. 10. The misorientation angle distribution of as-deformed (a, b) and annealed (c, d) grain structures for the single-step homogenization of 500°C/2h (a, c) and the two-step homogenization of 400°C/48 h + 500°C/2h (b, d).

Tables

Table 1: Chemical composition of the studied 6xxx alloy (wt.%).

Mg	Si	Fe	**Zr**	Ti	Al
0.40	0.35	0.18	**0.15**	0.13	Bal.

Table 2. Characteristics of Al_3Zr dispersoids inside the dispersoid zones after different homogenization treatments.

Homogenization	**Number Density, $\times 10^{21}$ m^{-3}**	**Average diameter, nm**
400°C/48h (first step)	2.8 ± 0.6	9.1 ± 0.8
500°C/2h	0.9 ± 0.2	13.7 ± 0.9
500°C/5h	1.0 ± 0.2	14.1 ± 0.7
400°C/48h + 500°C/2h	2.3 ± 0.4	10.3 ± 1.1
400°C/48h + 500°C/5h	1.7 ± 0.2	12.9 ± 0.9

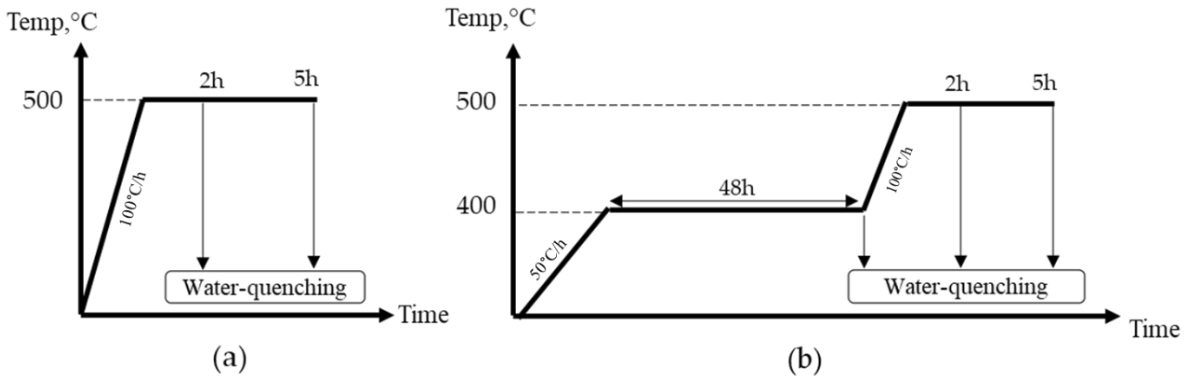

Fig. 1. Schematic diagrams of the homogenization treatments, (a) single-step and (b) two-step treatments.

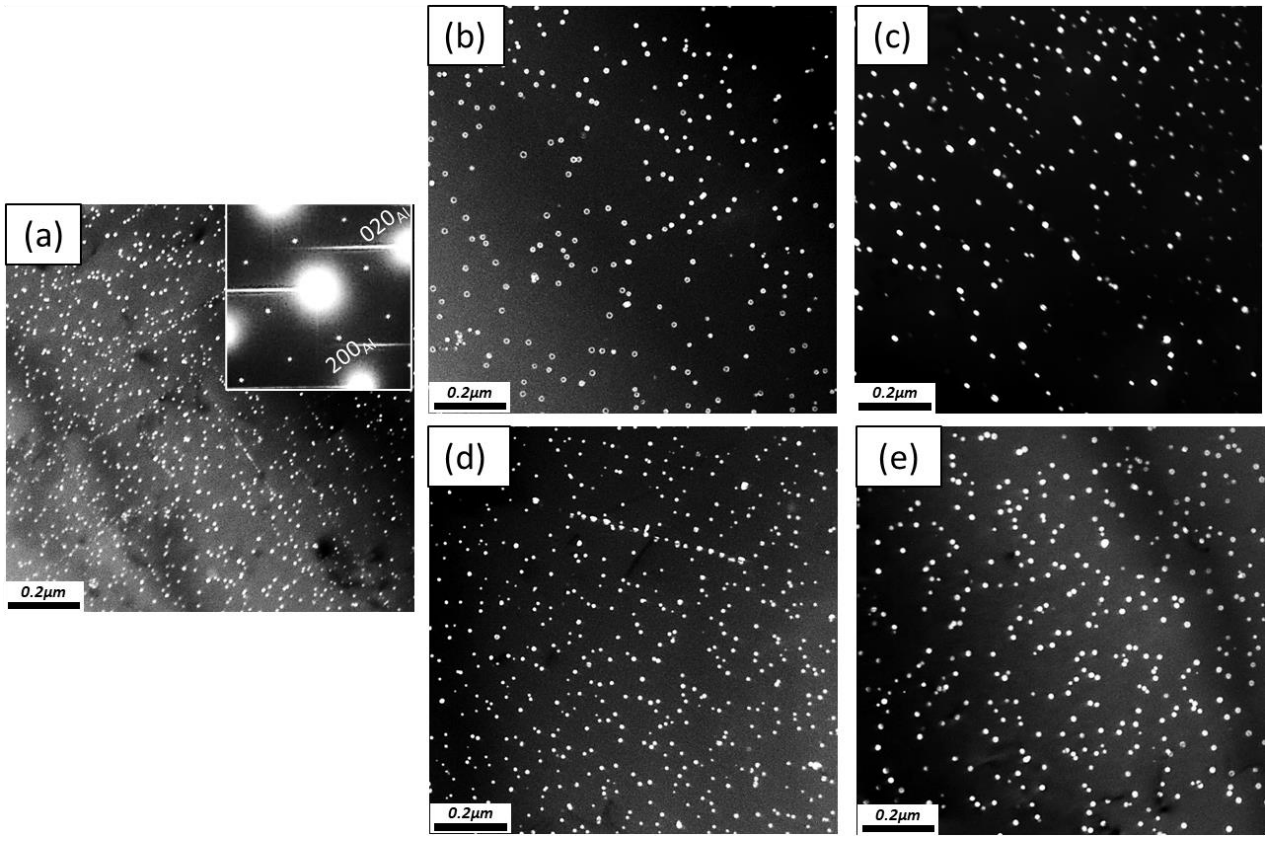

Fig. 2. TEM dark-field images of Al_3Zr dispersoids formed in the dispersoid zones after different homogenization treatments: (a) 400°C/48h (first step), (b) 500°C/2h, (c) 500°C/5h, (d) 400°C/48h + 500°C/2h and (e) 400°C/48h + 500°C/5h.

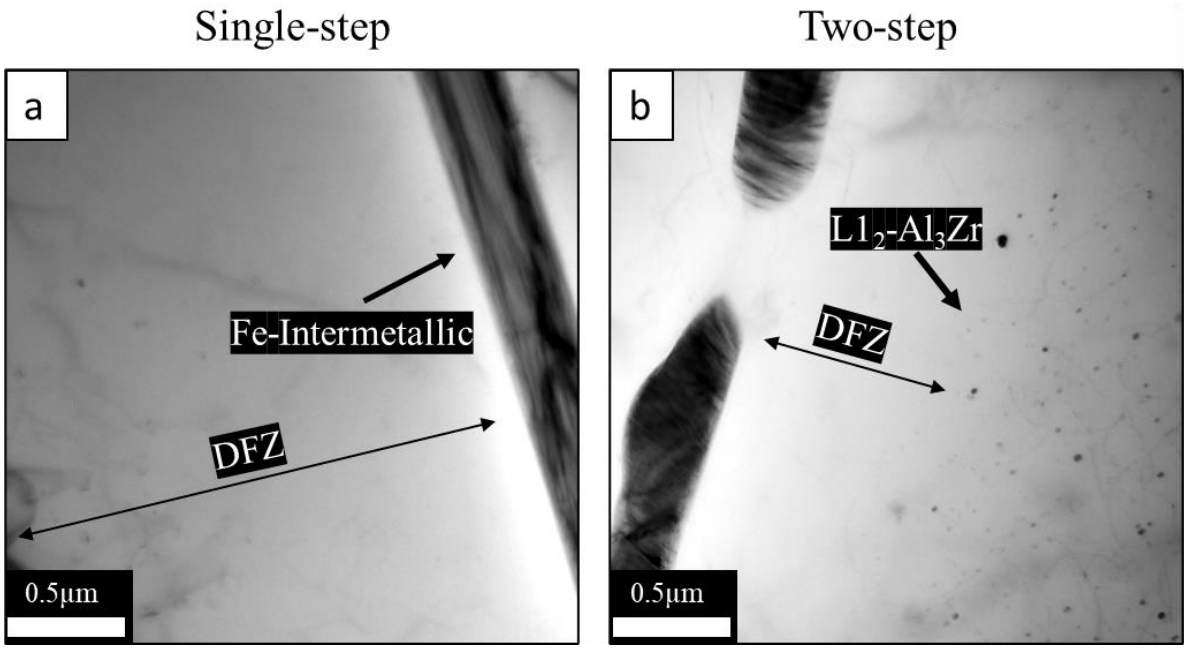

Fig. 3. Bright field TEM images near grain boundaries showing the width of DFZs in, (a) single-step 500°C/2h, and (b) two-step 400°C/48 h + 500°C/2h homogenization conditions. The Fe-intermetallic in (a) was identified as the plate-like β-AlFeSi intermetallic phase (see Fig. S4 in Supplementary Material).

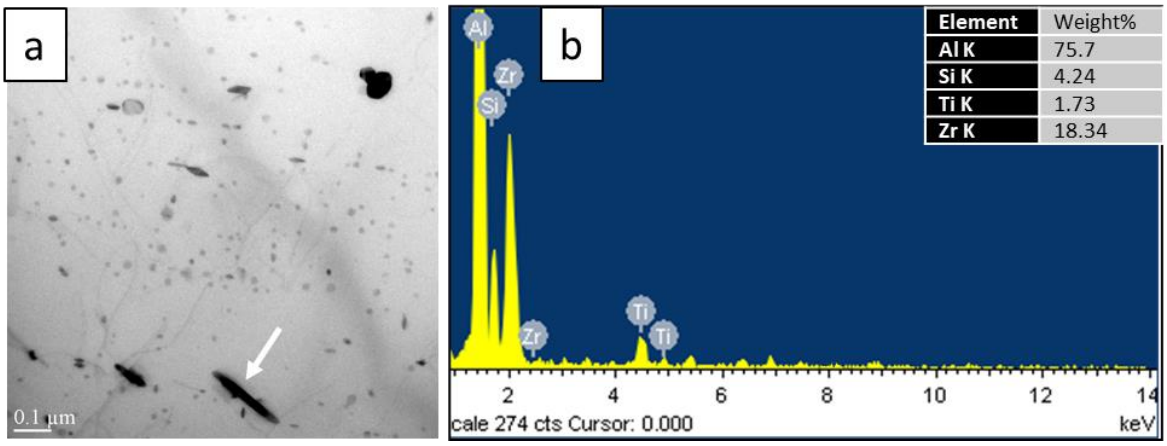

Fig. 4. (a) Bright field TEM image showing the elongated DO_{22}-$(Al,Si)_3(Zr,Ti)$ dispersoids and (b) the corresponding TEM-EDS spectrum.

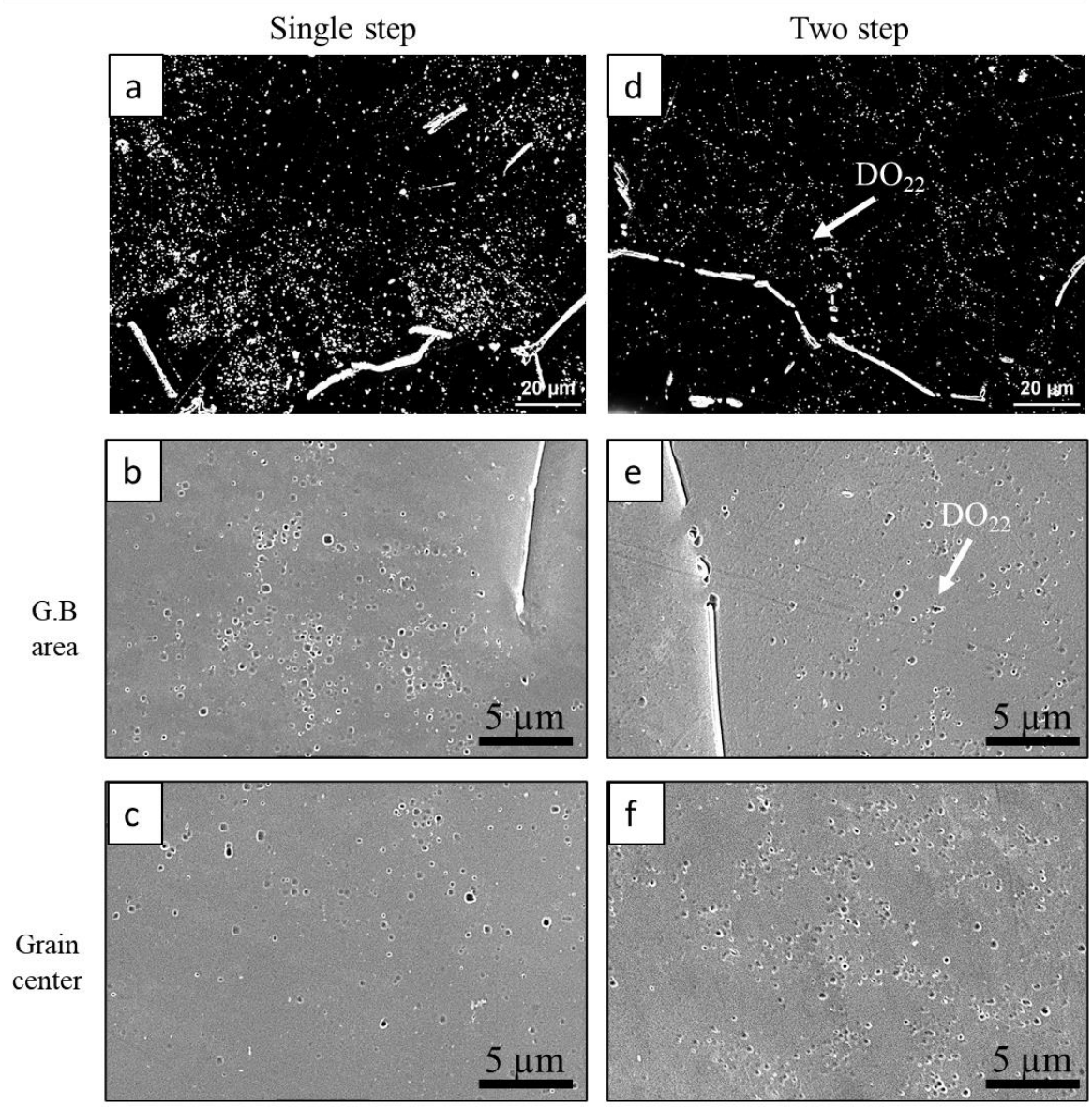

Fig. 5. Optical dark field and SEM images showing the distribution of the DO_{22}-$(Al,Si)_3(Zr,Ti)$ dispersoids for single-step 500ºC/5h (a-c) and two-step 400ºC/48h + 500ºC/5h (d-f) treatments.

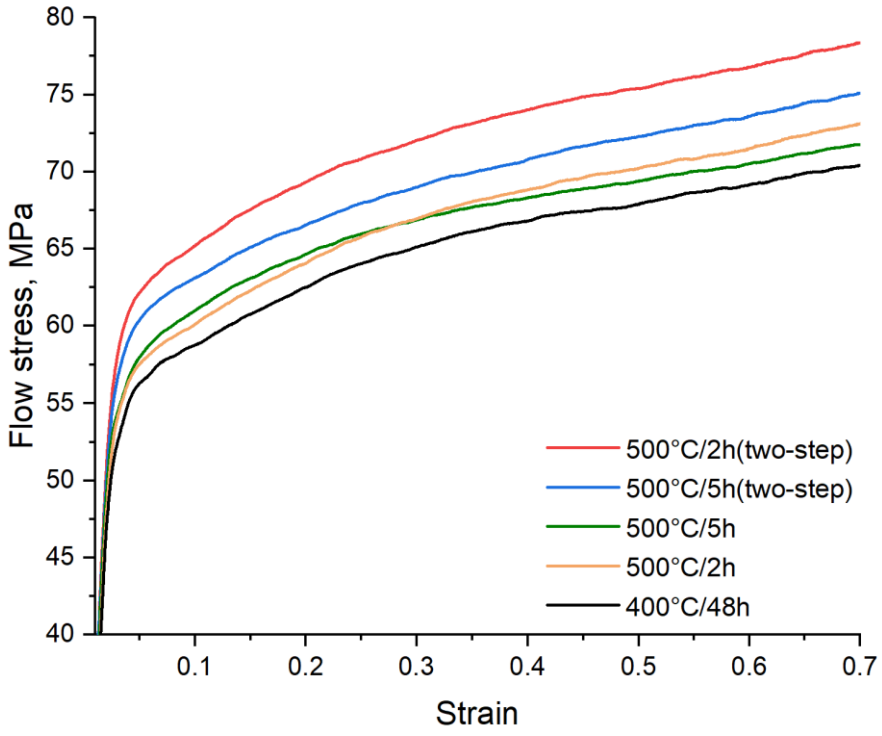

Fig. 6. Typical flow stress curves after deformation at 350 °C and 1.0 s^{-1} in different homogenization conditions.

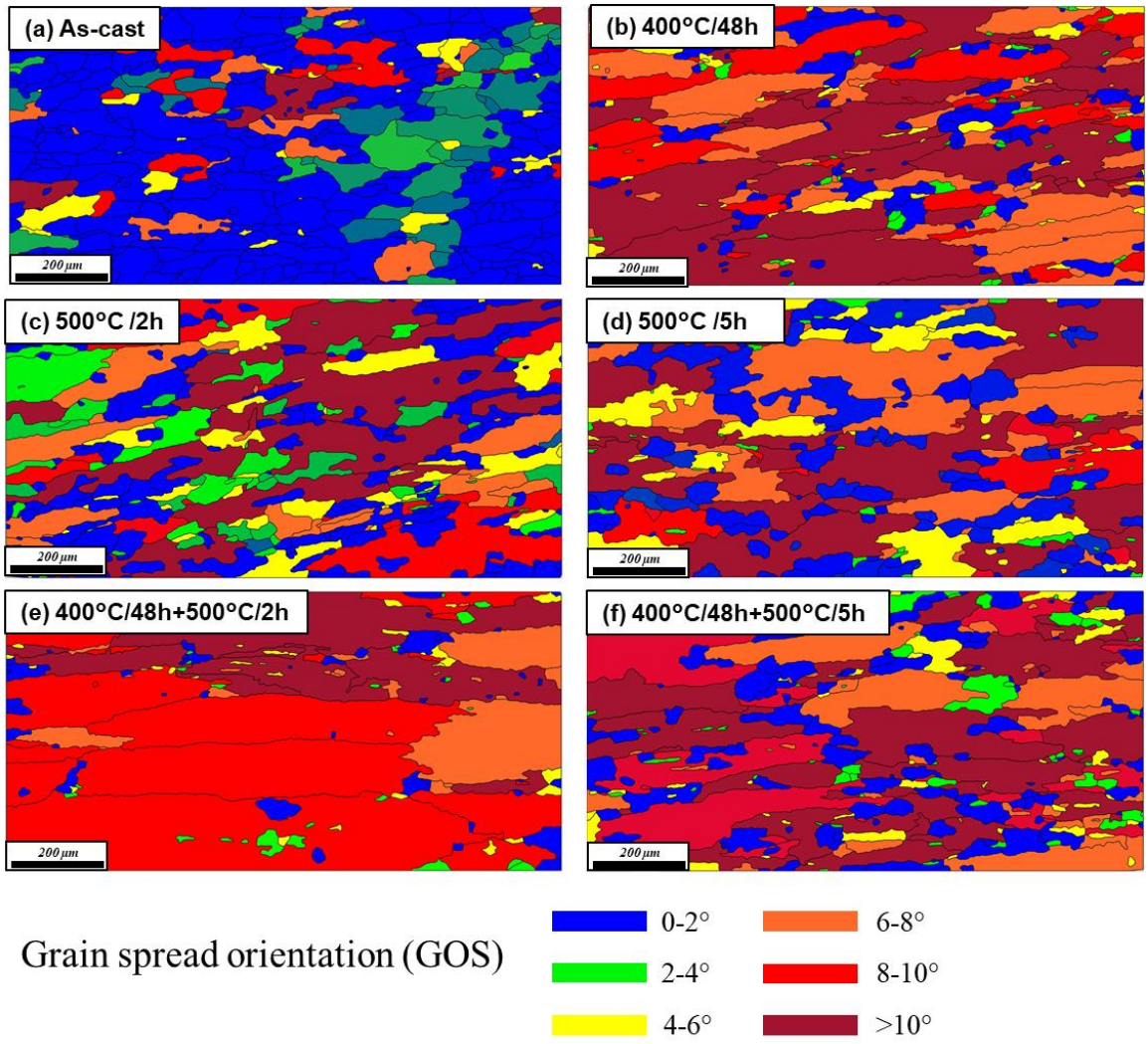

Fig. 7. Grain spread orientation maps for different alloy conditions after deformation at 350 °C and 1.0 s^{-1} and annealing at 500 °C for 1 h.

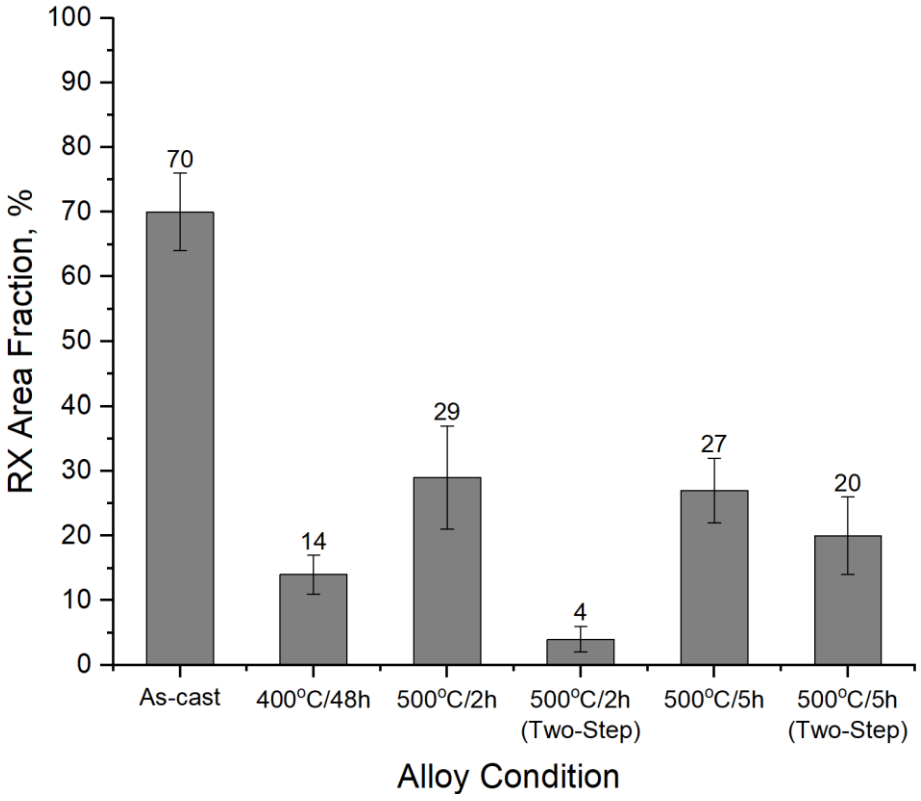

Fig. 8. Recrystallization area fraction for different alloy conditions after deformation at 350 °C and 1.0 s^{-1} and annealing at 500 °C for 1 h.

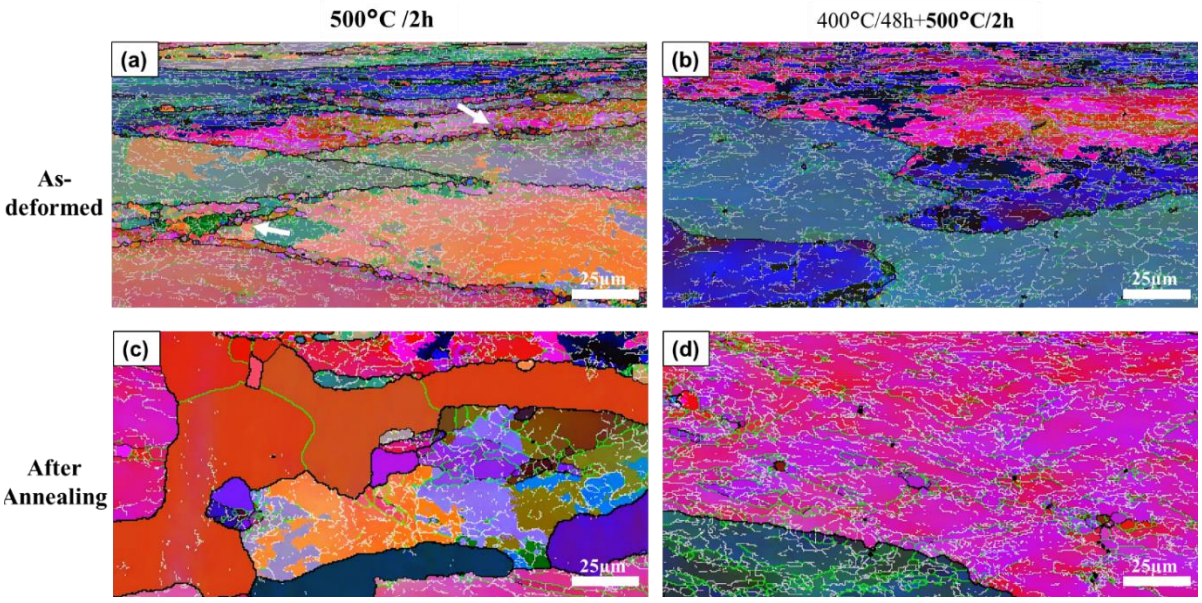

Fig. 9. All-Euler orientation maps of as-deformed (a, b) and annealed (c, d) grain structures for

the single-step homogenization of 500°C/2h (a, c) and the two-step homogenization of 400°C/48h + 500°C/2h (b, d). Low angle (2°-5°), medium angle (6°-15°), and high angle boundaries (>15°) are represented by white, green, and black lines, respectively.

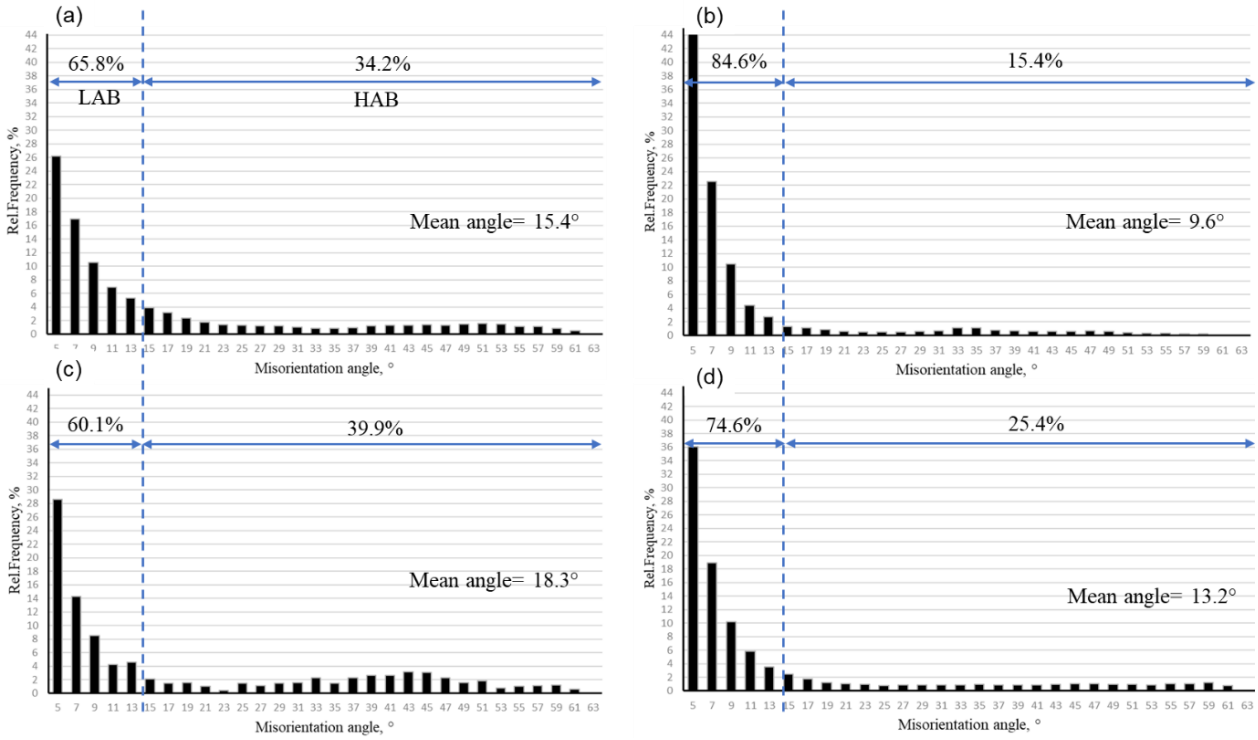

Fig. 10. The misorientation angle distribution of as-deformed (a, b) and annealed (c, d) grain structures for the single-step homogenization of 500°C/2h (a, c) and the two-step homogenization of 400°C/48 h + 500°C/2h (b, d).

Supplementary Material

For:

Improving the dispersoid distribution and recrystallization resistance of a Zr-containing 6xxx alloy using two-step homogenization

A. Elasheri [a,*], E.M. Elgallad [a], N. Parson [b], X.-G. Chen [a]

[a] Department of Applied Science, University of Quebec at Chicoutimi, Saguenay (QC), Canada G7H 2B1

[b] Arvida Research and Development Centre, Rio Tinto Aluminium, Saguenay (QC), Canada G7S 4K8

(*Corresponding author: ali.elashery1@uqac.ca)

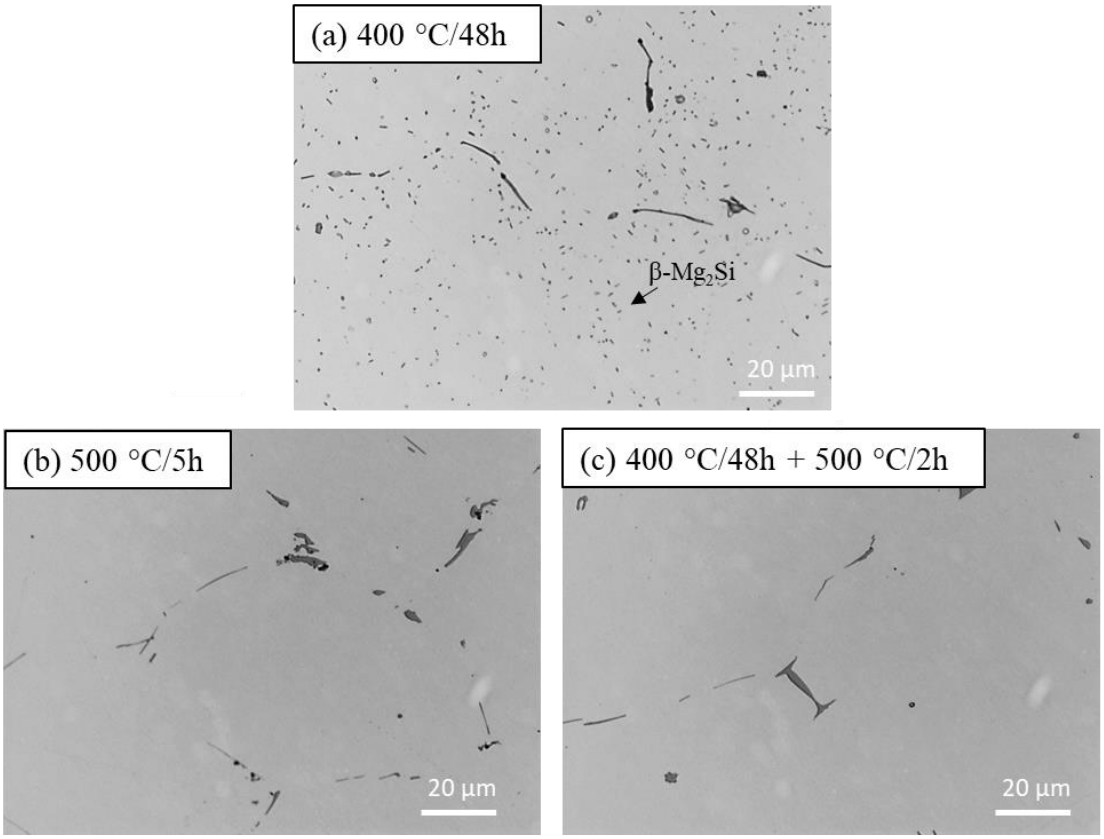

Fig. S1. Optical micrographs showing the presence and absence of β-Mg2Si precipitates in different homogenization conditions.

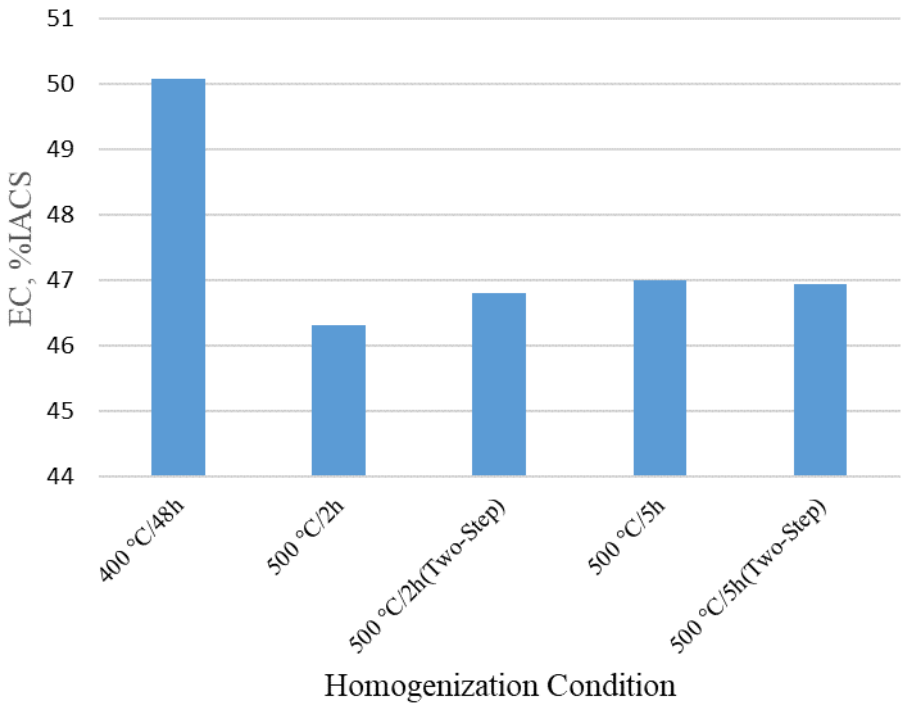

Fig. S2. Electrical conductivity (EC) of the alloy studied in different homogenization conditions.

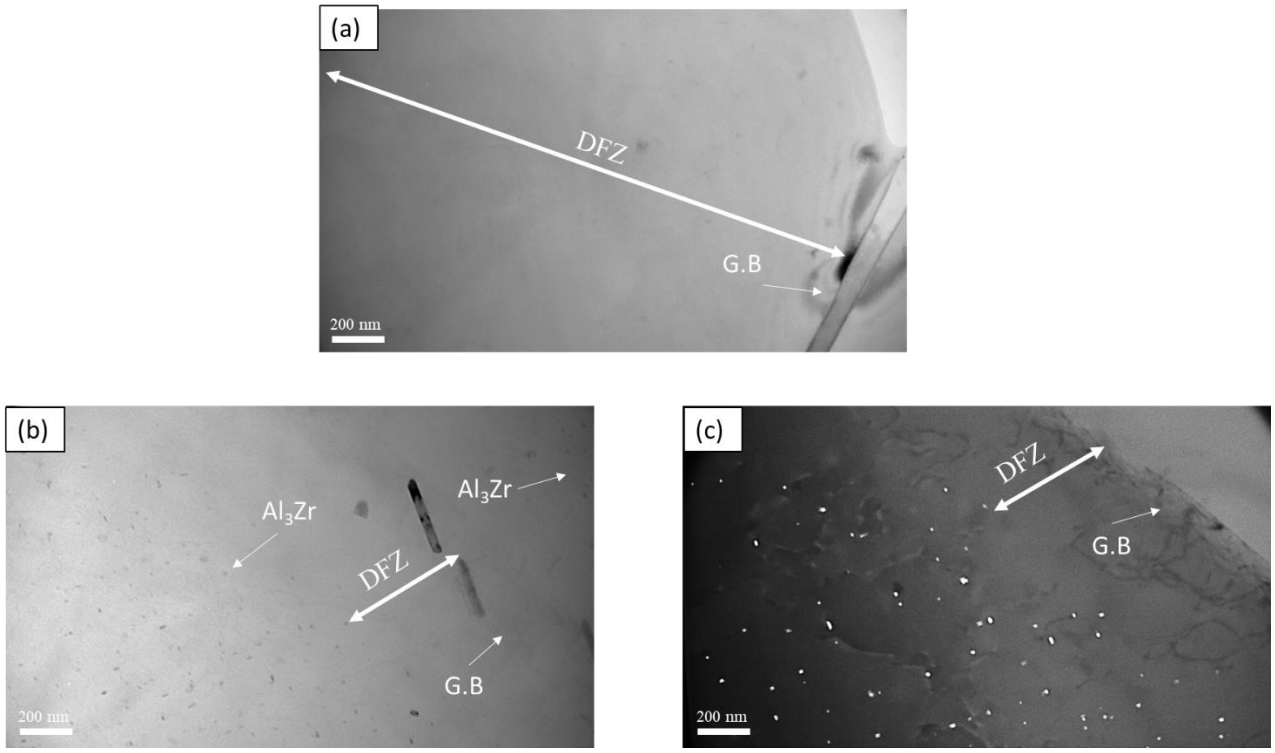

Fig. S3. TEM images showing the width of DFZs near grain boundaries in, (a) single-step 500°C/2h, and (b,c) two-step 400°C/48 h + 500°C/2h homogenization conditions.

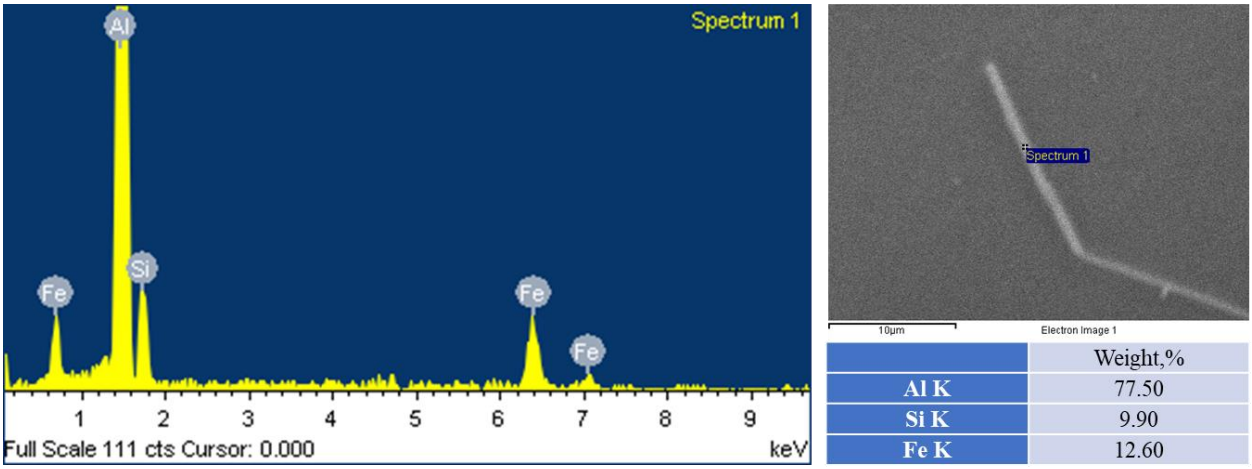

	Weight,%
Al K	77.50
Si K	9.90
Fe K	12.60

Fig. S4. SEM-EDS analysis of the plate-like β-AlFeSi intermetallic phase.